

SRC Project Annual Report

Task ID 425.025

Deliverable Name

PART I. Aggregation kinetics of semiconductor nanoparticles in the environmentally relevant water chemistries.

PART II. Benchmark data describing relationship between physicochemical properties and bilayer assay.

Task Title

Development of a Quantitative Structure-Activity Relationship for the Prediction of the Biological Effects of Nanoparticles Associated with Semiconductor Industries

Task Leader: Yongsheng Chen - Georgia Institute of Technology

Email: yongsheng.chen@ce.gatech.edu; Phone: 404-894-3089

Co-Task Ldr: Trevor Thornton and Jonathan Posner - Arizona State University

December 29, 2010

PART I. Aggregation kinetics of semiconductor nanoparticles in the environmentally relevant water chemistries.

Summary/Abstract

To develop a robust QSAR model capable of predicting toxicity of semiconductor nanomaterials, we need to gain insight into the key physicochemical properties that govern their environmental fate and transport. Characterizations of particle stability and aggregation are essential for understanding their environmental and biological impacts (1-4) and are also the basis for validating and normalizing the results of different toxicity experiments (5-7). Aggregation of AgNPs changes particle size and morphology, which may significantly influence the biological interactions (e.g., the ability of translocation across the cell membrane surfaces) and thus the antibacterial activity (8, 9). To this end, we studied the aggregation kinetics of CeO₂ nanoparticles and silver nanoparticles (AgNPs) and on the basis of our results we observed that particle size, surface tension, environmental conditions (e.g., pH, ionic strength and temperature) are all important for the aggregation kinetics. The unique feature of AgNPs is that under the open and closed systems they exhibited different aggregation kinetics, which is largely ascribed to the oxidation of silver and the subsequent silver ion release and speciation in open systems. It is found that aggregation rates in open systems were much greater than those in close systems; and small AgNPs had a higher aggregation rate than large AgNPs. **In summary, three papers have been published; three manuscripts are under revision; and two manuscripts were submitted under this project.**

Technical Results and Data

1. Aggregation kinetics of CeO₂ nanoparticles and modeling analysis

1.1. Characterizations of CeO₂ NPs

The wide range of applications of silver nanoparticles (AgNPs) in food processing, clothing and other household products provides many opportunities for their release into the environment (4, 9-12). There is much evidence of NP toxicity to bacteria (13, 14), aquatic organisms (15, 16), and mammalian cells (17-20), which makes it imperative to understand the likelihood of the exposure, fate, transport, and transformation of AgNPs in complex and realistic environmental matrices (21, 22).

Aggregation kinetics of CeO₂ nanoparticles (NPs) was studied by time-resolved dynamic light scattering (TR-DLS) experiments and the data was interpreted with Derjaguin–Landau–Verwey–Overbeek (DLVO) theory and. Figure 1a shows the zeta potential over different pHs and Figure 1b shows the particle size distribution (PSD) diagram of CeO₂ NPs dispersed in suspension with a concentration of 1 g/L and the mean hydrodynamic diameter was approximately 190 nm with the polydispersivity index (PDI) of 0.18. The morphology of CeO₂ NPs was studied by AFM and Figure 1c and 1d show the topography images of CeO₂ NPs in dense and scattered states. CeO₂ NPs were close to spherical in shape with a relatively uniform size distribution. These images may reflect the morphologies of CeO₂ NPs as aggregates and individual particles, respectively. The size of CeO₂ NPs was approximately 20 - 25 nm as measured from these AFM images, which is consistent with the vendor's data.

To investigate the effect of ionic strength on aggregation kinetics, pH was kept constant at 5.6 and the ionic strength of the solution changed. Figure 2a shows that the hydrodynamic diameters increased fastest at the highest ionic strength (0.1 M), with the speed decreasing as ionic strength decreased. Clearly, at pH 5.6 and low ionic strength (0.002 ~ 0.01 M), electrostatic repulsion dominated, and thus almost no aggregation was observed during the experimental period. Overall, high ionic strength (0.025 ~ 0.1 M) led to a high aggregation rate. The increased particle aggregation rate at high ionic strength (0.025 ~ 0.1 M) was caused by a decrease in the repulsion or energy barrier. This can be verified by calculating the interaction energy profiles with DLVO theory. The total interaction energy was calculated by classic DLVO theory with the Eq. (1a).

1.2. The discrepancy classic DLVO theory in predicting aggregation kinetics

Figure 2b shows that at the ionic strength below 0.005 M, a large energy barrier prevented aggregation. For example, according to the TR-DLS data, aggregation could barely occur at the ionic strength of 0.002 M. In contrast, with an ionic strength above 0.005 M, the energy barrier diminished greatly, and aggregation of CeO₂ NPs could occur instantly. This prediction is consistent with the aggregation experiments for 0.025 M and 0.1 M. However, at 0.005 M and 0.01 M, the associated energy barriers were nearly zero or even negative, but the anticipated aggregation was not observed at all. These discrepancies between DLVO predictions and experimental results have also been reported in other studies (23-26) and ascribed to several likely causes, as mentioned in the introduction. One simple explanation is that DLVO does not consider surface heterogeneity (27-30). Classic DLVO theory treats the interacting surface as an infinitely smooth surface (i.e., molecularly smooth), which does not actually exist (30-33). Thus, the aggregation attachment efficiency α (otherwise known as the inverse stability ratio, $1/W$), derived from the DLVO theory was also found to deviate from the slopes of experimental aggregation curves, as reported previously (34, 35).

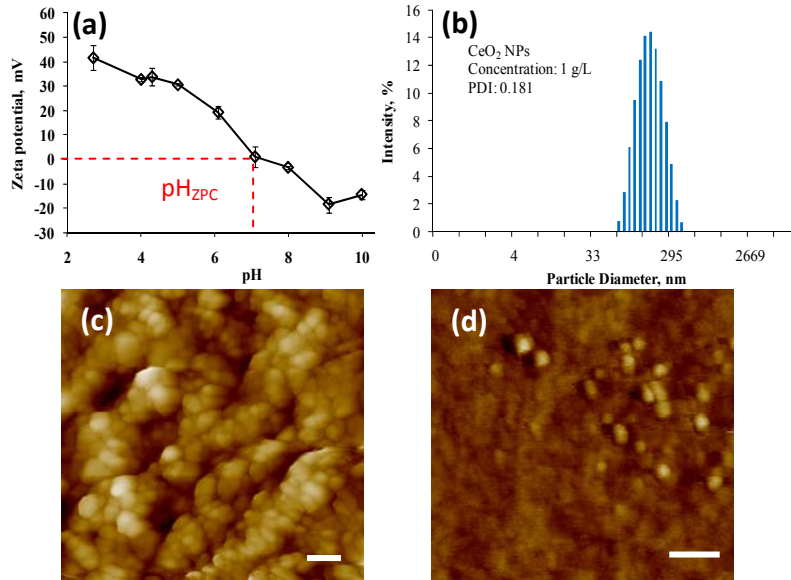


Figure 1 (a) Particle size distribution of CeO₂ NPs in DI water with a concentration of 1 g/L. (b) Zeta potential under different pH with 0.01 M KCl as the reference electrolyte. (c) and (d) AFM images of CeO₂ NPs in dense and scattered states. The white scale bar is equal to 50 nm in (c) and 30 nm in (d).

1.3. Modeling the aggregation kinetics

To overcome the DLVO discrepancy from experimental observations, we employed EDLVO which considers the acid-base interaction to account for the non-DLVO effects. Moreover, we also related the activation energy (E_a) in Arrhenius form to the energy barrier (E_b) in the DLVO interaction energy (36). This relation assumes aggregation as a 2nd-order chemical reaction with monosized CeO₂ NPs as the reactants in the initial aggregation stage. Below equation is the aggregation rate (equivalent to the reaction rate) using Arrhenius equation:

$$r_c = KC_A^2 = 4\sqrt{3}(K_B T)^{1/2} R(t)^{1/2} \rho^{-1/2} N_A^{1/2} \exp\left(\frac{-|E_b - \phi_{\min 2}|}{K_B T}\right) C_A^2 \quad (1)$$

C_A^2 is further expressed as:

$$C_A^2 = \left[\frac{M}{\rho \frac{4}{3} \pi R(t)^3} \right]^2 \quad (2)$$

where M is the mass concentration of CeO₂ NPs initially applied in the aggregation experiment, which was a constant (10 mg/L) in all TR-DLS experiments. Substituting (2) into (1) yields:

$$r_c = \frac{9\sqrt{3}}{4} \pi^{-2} M^2 (K_B T)^{1/2} \rho^{-2.5} N_A^{0.5} R(t)^{-5.5} \exp\left(\frac{-|E_b - \phi_{\min 2}|}{K_B T}\right) \quad (3)$$

This equation is named the Arrhenius-EDLVO kinetics equation, and except for $R(t)^{-5.5} \exp\left(\frac{-|E_b - \phi_{\min 2}|}{K_B T}\right)$, all the other terms can be treated as constants. $|E_b - \phi_{\min 2}|$ can be obtained from the interaction energy profile given that the particle radius $R(t)$ is fixed and 1.5 mJ/m² is used for $\Delta G_{iwi, D_0}^{AB}$. Eq. (3) was used to analyze the aggregation kinetics of CeO₂ in Figure 3a, which has a common feature in different kinetic periods of aggregation: stage 1 (linear growth stage), stage 2 (deceleration growth stage), and stage 3 (stationary growth stage). During stage 1, the hydrodynamic radius grew almost linearly from the initial 100 nm to approximately 280 nm, and the aggregates were nearly monosized, as seen from the narrow distribution of data points. In stage 2, a transition state, the aggregation rate decreased because the hydrodynamic radius increased more slowly than in stage 1. In stage 3 the particle radius growth almost ceased, and the PSD became more scattered.

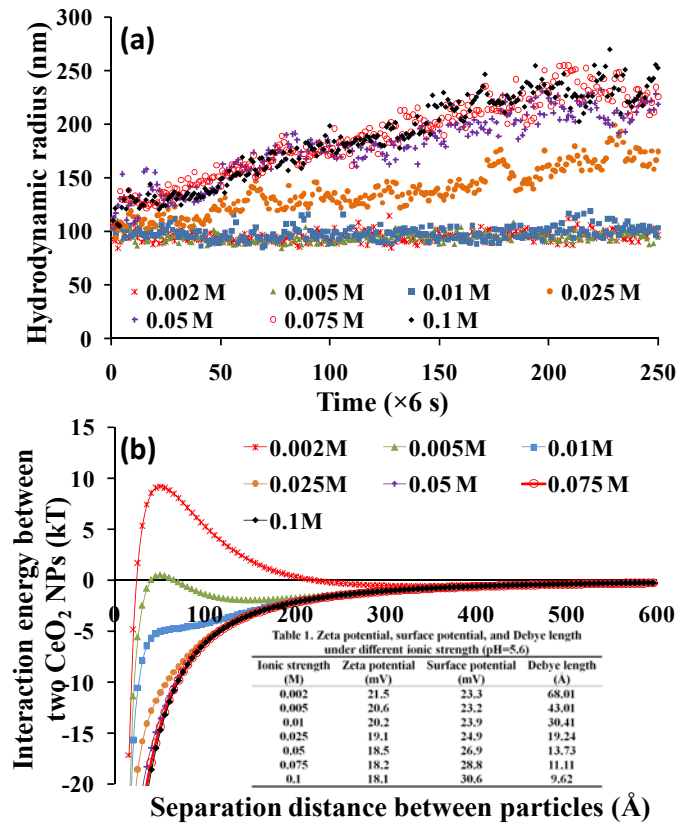


Figure 2. (a) Aggregation kinetics of CeO₂ NPs under different ionic strengths. (b) Interaction energy between CeO₂ NPs under different ionic strengths calculated from classic DLVO theory. In the bottom right of (b), Table 1 presents important parameters used in the interaction energy calculation.

Five particle radii were randomly chosen from each stage to calculate the aggregation rate (r_C) with Eq. (7); these rates which are shown in the left Y-axis of Figure 3b. The aggregation rate constant (K) was also calculated and is shown on the right Y-axis of Figure 3b. The slopes corresponding to these different radii were readily measured from the aggregation kinetics curves in Figure 3a and are shown on the X-axis. Plots of the aggregation rates or rate constants versus the slopes of the hydrodynamic radii are shown in Figure 3b. Higher aggregation rates and rate constants correspond to larger slopes, which is congruent with the experimental data in Figure 3a. The fitting equations indicate that the slopes were correlated to the calculated aggregation rates and the rate constants in exponential functions ($y=346.75e^{14.268x}$) and ($y=5E-06e^{8.9423x}$), respectively, with the correlation coefficients (R^2) of 0.9776 and 0.9644. This is probably reasonable because according to the Rayleigh-Gans-Debye approximation (37, 38), the slope of the aggregation kinetics curve is only equivalent to the aggregation rate for primary particles that are relatively small compared to the incident wavelength. In contrast, with the Arrhenius-EDLVO kinetics equation, we derive the potential relations between the slope and aggregation rate or rate constant at each stage, not merely the initial aggregation phase.

In stages 2 and 3, the approximation of monosized CeO₂ NPs in the aggregates seems not to hold, based on Figure 3a. However, the top of Figure 3a shows a typical PSD diagram and the mean radius chosen from each stage (101, 300, and 407 nm). In contrast to the hydrodynamic radius curve below, the PSDs give better statistical distributions of the particle sizes in suspension. Based on their PDI values, which were less than 0.5, CeO₂ NPs in stages 2 and 3 are still considered to be monodispersed. Thus, the calculated aggregation rates still correlated well with the slopes (in the low value range) as Figure 3b shows.

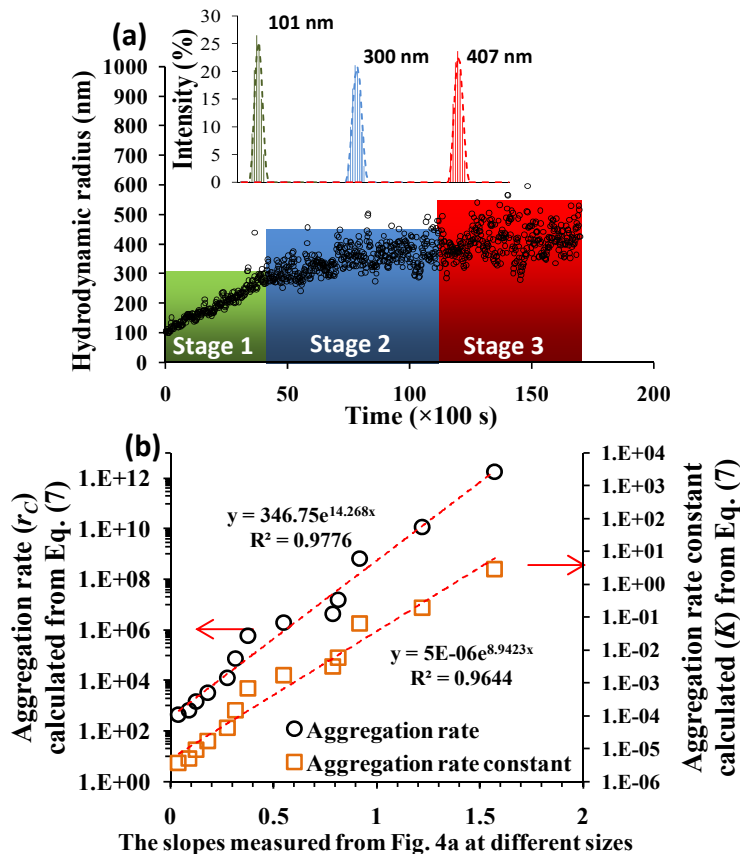


Figure 3. (a) Aggregation kinetics curve of CeO₂ NPs at an ionic strength of 0.02 M. Black datapoints represents the hydrodynamic radius at each reading by the DLS On the top are PSD diagrams at the three stages. (b) Aggregation rates calculated from Eq. (3) versus the slopes measured from the above aggregation kinetics curve at different aggregation stages. The radii in aggregation stage 1 include 100, 150, 200, 250, and 280nm; stage 2:290, 300, 330, 360, and 390 nm; and stage 3: 400, 410, and

420 nm. The calculated aggregation rate on the left Y-axis has the unit of $\frac{9\sqrt{3}}{4} \cdot 10^{-25} \cdot \pi^{-2} M^2 (K_B T)^{1/2} \rho^{-2.5} N_A^{0.5}$, the calculated aggregation rate constant on the right Y-axis has the unit of $\frac{9\sqrt{3}}{4} \cdot 10^7 \cdot \pi^{-2} M^2 (K_B T)^{1/2} \rho^{-2.5} N_A^{0.5}$, and the slope on the X-axis has the unit of $\left[\frac{dR(t)}{dt} \right]$. All the terms in the above equations use SI units.

1.4. Modeling the ionic strength effect on the aggregation kinetics

To further validate the applicability of Arrhenius-EDLVO kinetics equation, we investigated the effect of ionic strength on aggregation kinetics, the aggregation kinetics data under the ionic strengths of 0.01, 0.02, 0.025, 0.05, 0.075, and 0.1 M in Figure 2a and Figure 3a were used. Three typical aggregate radii (125, 160, and 200 nm) were chosen for the calculation. For each aggregate radius, the slopes corresponding to different ionic strengths were measured directly from the aggregation kinetics curves. The same three radii were used to calculate aggregation rates, and 1.5 mJ/m^2 was again used for $\Delta G_{iwi, D_0}^{AB}$. The total interaction energy profiles under the six ionic strengths are shown in Figure 4a. Ionic strength clearly caused the interaction energies of the same-sized CeO₂ NPs to have different energy barriers (E_b) and secondary energy minima ($\phi_{\min 2}$). Thus, the variations of $|E_b - \phi_{\min 2}|$ with ionic strength could be determined from Figure 4a, which presents a typical interaction energy profile for the radius of 125 nm. The Arrhenius-EDLVO kinetics equation was then used to calculate aggregation rates for the three radii under different ionic strengths. Figure 4b shows that the slopes had exponential relationships with the calculated aggregation rate, as indicated by the fitting equations. The data points in Figure 4b represent ionic strengths from 0.01 M to 0.1 M. Thus, a high ionic strength (e.g., 0.1 M) led to a high aggregation rate and a steeper slopes of the aggregation curves. This is reasonable because high ionic strength lowers the energy barrier and thus promotes the aggregation rate according to Eq. (7). As the aggregate radius increased from 125 nm to 200 nm, the slopes and the calculated aggregation rates decreased for each ionic strength, which is in agreement with experimental observations.

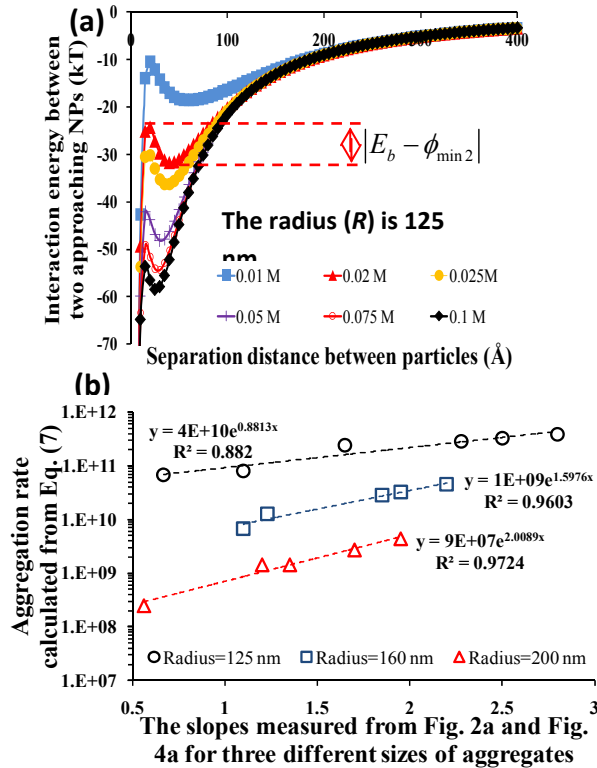


Figure 4. (a) Total interaction energy profiles under different ionic strengths as calculated by EDLVO theory. (b) Aggregation rates calculated from Eq. (7) versus the slopes measured from the aggregation kinetics curves under different ionic strengths as marked beside the data points. The aggregation rate on the Y-axis has the unit of $\frac{9\sqrt{3}}{4} \cdot 10^{-25} \cdot \pi^{-2} M^2 (K_B T)^{1/2} \rho^{-2.5} N_A^{0.5}$ and the slope on the X-axis has the unit of $\left[\frac{dR(t)}{dt}\right]$. All the terms in the above equations use SI units.

1.5. Modeling the temperature strength effect on the aggregation kinetics

As Arrhenius equation is commonly used to describe the temperature effects on reaction rates (39), we further extended this equation in predicting the temperature dependence of CeO₂ as well as two other metal oxide NPs (CuO and Fe₂O₃) that has a certain relevance for semiconductor industries. According to the Arrhenius-EDLVO kinetics equation in Eq. (3), increasing the temperature will exponentially decrease the aggregation rate. Our experimental observations in Figure 5 matched this model prediction.

In summary, the Arrhenius-EDLVO kinetics model we developed agreed with the experimental results and this model potentially can predict and analyze the stability and aggregation kinetics of NPs in aqueous solution without carrying out TR-DLS experiments. The primary factors to consider include particle size, surface charge, surface tension, ionic strength, and $\Delta G_{twl, D_0}^{AB}$.

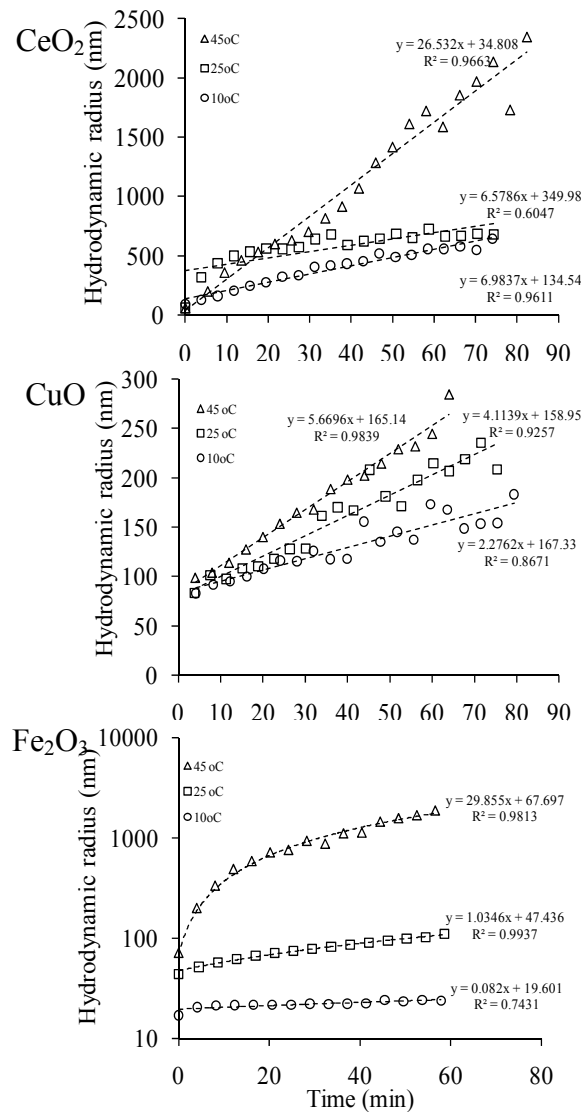


Figure 5. Temperature effects on aggregation kinetics of CeO₂, CuO and Fe₂O₃ (hematite) NPs

2. Aggregation kinetics of silver nanoparticles in open and closed systems

The wide range of applications of silver nanoparticles (AgNPs) in food processing, clothing and other household products provides many opportunities for their release into the environment (4, 9-12). There is much evidence of NP toxicity to bacteria (13, 14), aquatic organisms (15, 16), and mammalian cells (17-20), which makes it imperative to understand the likelihood of the exposure, fate, transport, and transformation of AgNPs in complex and realistic environmental matrices (21, 22).

In open systems, different physiochemical processes may occur concurrently with aggregation, including mass transfer of oxygen and carbon dioxide between the gas and liquid phases, oxidation of silver metals, silver ion release, speciation of silver ions, and equilibrium between precipitation and dissolution (40). In contrast, a closed system (anoxic and anaerobic conditions) imposes a low redox potential, and thus oxidation processes may be inhibited or slowed. A considerable level of AgNPs likely enters deep soils, river sediments, and underground water, where anaerobic conditions dominate and AgNPs could avoid oxidation and reside longer than in aerobic conditions. Bacteria (especially nitrogen-fixing heterotrophic and soil-forming chemolithotrophic bacteria) provide important ecological functions and fundamental services, such as nitrogen cycling, to ecosystems. The persistence of AgNPs may adversely affect beneficial bacteria and disrupt ecological functions. *In situ* studies have demonstrated that silver, even in larger particle form, inhibits microbial growth at concentrations less than those of other heavy metals as well as disrupts denitrification processes (41), which means that silver has the potential to cause ecosystem-level disruption. Similarly, evidence shows that AgNPs can enter and accumulate in the gastrointestinal (GI) tract of the human body and disrupt the intestinal microbial functions, resulting in irritation or disorders of the digestive system (9, 42-44). As mentioned earlier, aggregation is an important environmental behavior that may be linked with the fate and biological interactions of AgNPs. However, no study has investigated or compared the aggregation kinetics of AgNPs in open and closed systems yet.

2.1. Characterizations of AgNPs

Figure 6a shows the morphology of AgNPs we used, which were spherical in shape with a relatively uniform size distribution of 40-65 nm and consistent with the manufacturer's reported size. The inset of Figure 6a is a PSD histogram of 40-nm AgNPs immediately after dispersal in DI water. The peak intensity corresponds to approximately 43 nm, which agrees with the diameter determined from AFM. The DLS system reported a Polydispersivity Index (PDI) value of 0.19 for the AgNP suspension and a PDI value between 0.1 and 0.25 indicates that the NPs are polydispersed in the suspension with a narrow particle size distribution and without significant aggregation or sedimentation. To determine the surface charge, ζ -potential was measured under different pH values. The relationships between ζ -potential and suspension pH for the three NP sizes are shown in Figure 6b. The zero points of charge (ZPC) for all AgNP sizes were approximately pH 2, at which AgNPs are neutrally charged and highly unstable. In the aggregation experiments, the pH was approximately 5.6 (in both DI water and the Hoagland medium), and thus the AgNPs were negatively charged according to Figure 6b. This result agrees with the reported ζ -potential of -50 mV for citrate-coated AgNPs with a mean diameter of 4.8 nm (45).

2.2. Attachment efficiency (α) and critical coagulation concentration (CCC)

Time-resolved dynamic light scattering (TR-DLS) experiments indicated that aggregation of 20- and 40-nm AgNPs exhibited apparent reaction-limited (slow) and diffusion-limited (fast) regimes under different ionic strengths. The effect of electrolyte addition on particle aggregation kinetics was previously discussed and is mainly attributed to the compression of the outer shell of the electrical double layer and the decrease in the magnitude of the ζ -potential (46, 47). As a result, the inter-particle repulsion from electrostatic force is reduced, and thus the particle aggregation is greatly promoted. We confirmed this by measuring ζ -potentials of the three sizes of AgNPs at different KNO_3 concentrations (results are shown here). For 20- and 40-nm

AgNPs, increasing KNO_3 concentrations apparently led to a transition from unfavorable (low α) to favorable (high α) aggregation regimes, which is congruent with previous aggregation studies of metal NPs (40, 47-49). Because 80-nm AgNPs did not have notable aggregation during the initial 30 min, the attachment efficiency was shown as zero in Figure 7. The estimated CCC from Figure 7 was approximately 100 mM (KNO_3) for both 20- and 40-nm AgNPs, which did not show significant particle size dependency.

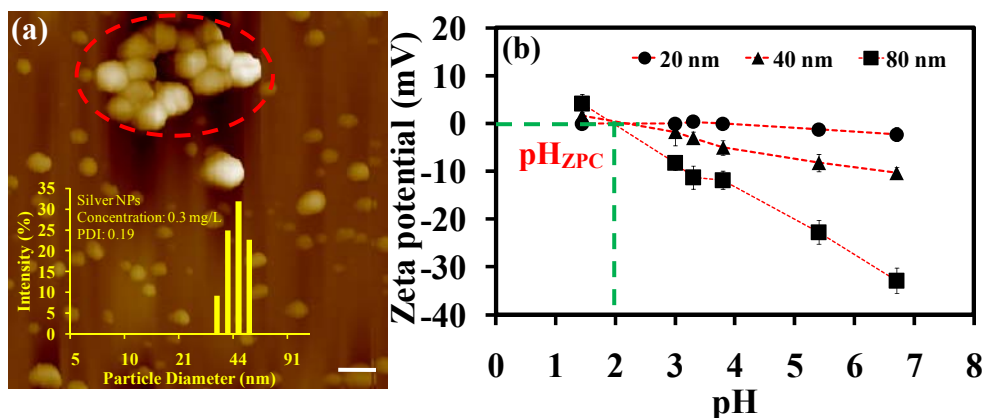


Figure 6 (a) Images of AgNPs acquired from AFM (the white scale bar at the bottom right is equal to 100 nm); the inset is a histogram of particle size distribution. (b) ζ -potentials for different sizes of AgNPs under different pH levels with 0.001 M KNO_3 as the reference electrolyte.

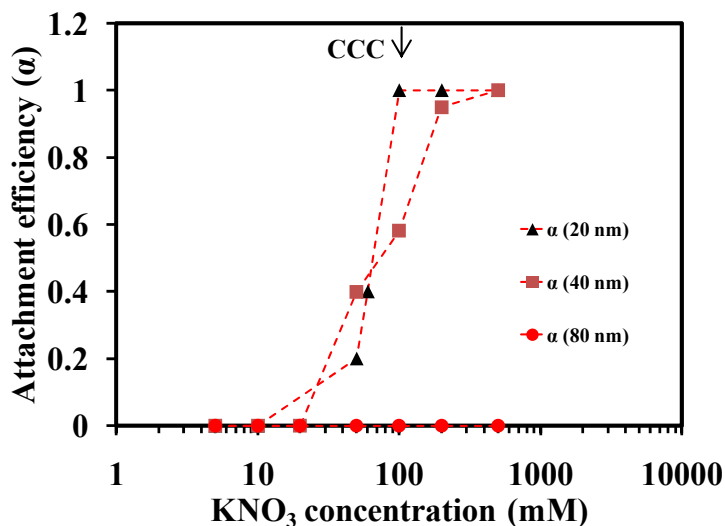


Figure 7 Experimental data on attachment efficiencies (α) and the calculated inverse stability ratios (I/W) for AgNPs as a function of KNO_3 concentration (pH 5.6). The critical coagulation concentration (CCC) is based on the intersection of the extrapolations of the unfavorable and favorable regimes, as marked by the black arrows. The estimated CCC for 20-, 40-, and 80-nm AgNPs were approximately 100, 75, 50 mM KNO_3 .

2.3. Aggregation kinetics of AgNPs in the quarter-strength Hoagland medium in open and closed systems

Fig. 8 compares the aggregation kinetics in open and closed systems for three sizes of AgNPs at two initial mass concentrations (300 and 600 $\mu\text{g/L}$). The graphs in the left and right columns are the hydrodynamic radius changes in open and closed systems, respectively. Clearly, the two systems share some common features, as well as some apparent differences.

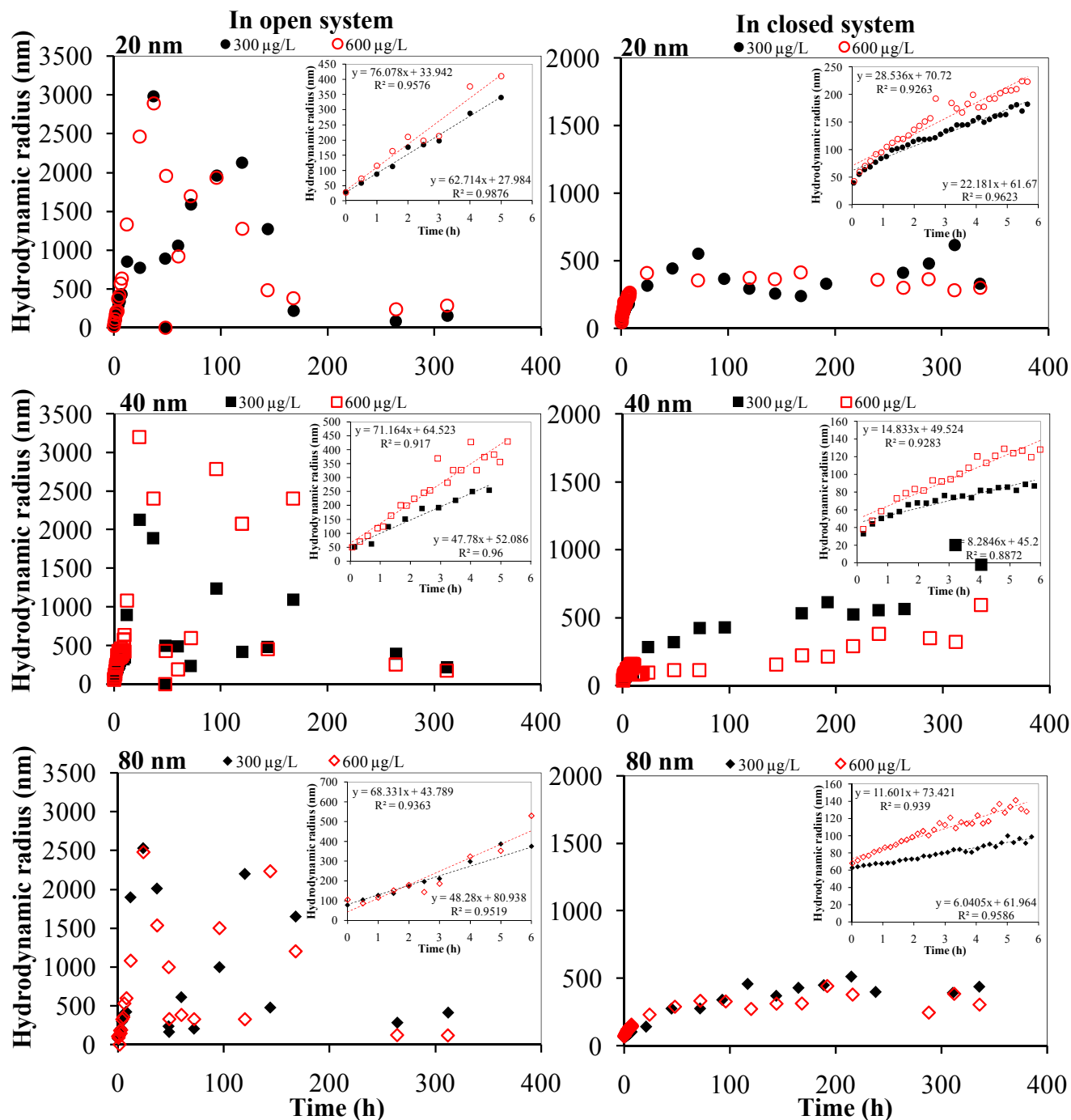


Figure 8. Aggregation kinetics of different sizes of AgNPs in Hoagland medium. The data in the left column represent the changes in hydrodynamic radii of AgNPs in open systems, while the data in the right column represent the changes in hydrodynamic radii of AgNPs in closed systems. The insets show the linear growth of the hydrodynamic radii.

In both systems, the hydrodynamic radii for all NP sizes increased almost linearly within the initial 4~6 h. After that, hydrodynamic radius changes became random and trendless in open systems. The effects of

particle size and particle concentration on aggregation rates were similar in both systems. The slopes (dr_H/dt) of the hydrodynamic radius curves during the linear growth stage, as obtained by the curve fits, indicate the aggregation rates. These are shown in the insets of each graph in Figure 8. For easy comparisons, Table S1 summarizes the slopes of the fitted curves. In both open and closed systems and at both initial concentrations, 20-nm AgNPs had much steeper slopes than did 40- and 80-nm AgNPs, which is consistent with previous findings on particle size effects on the aggregation kinetics of hematite NPs (50). Moreover, increasing the initial concentration from 300 to 600 $\mu\text{g/L}$ significantly increased the aggregation rates for all three sizes of AgNPs by approximately 21%-49% in open systems and 28%-93% in closed systems, respectively.

Figure 8 also shows differences in the aggregation kinetics of open and closed systems. After 50 to 150 h in an open system, the hydrodynamic radii of all sizes of AgNPs began to decline, probably because of disaggregation and oxidation of AgNPs. In contrast, the hydrodynamic radii in closed systems smoothly increased and exhibited features of salt-induced aggregation common to other metal NPs (47, 50, 51). The most striking difference between open and closed systems is that the aggregation rates were faster in open systems by approximately 3-8 times, as indicated by the slopes shown in the insets. As a result, AgNPs persisted for a longer time in closed systems than in open systems, and Figure 78 shows that the sizes of AgNPs in closed systems did not decline during the experiments.

The ionic strength (I) of the quarter-strength Hoagland medium was approximately 9.1 mM, which was determined by the equation $I=0.5\cdot\sum c_i Z_i^2$ (where c_i is the molar concentration of one ionic species (i), and z_i is the valency of the i^{th} ion). Compared to the CCC (100 mM KNO_3) in Figure 7, the aggregation of AgNPs in the Hoagland medium should be reaction-limited during the linear stage of aggregation. One may argue that the Hoagland medium contains different divalent and monovalent cations such as Ca^{2+} and Mg^{2+} , which may be more significantly effective in inducing AgNP aggregation than monovalent ions (K^+) (46). However, the total ionic strength of the Hoagland medium is relatively low and thus the effects of divalent cations on aggregation state can be negligible.

2.4. Implications of AgNP aggregation for aquatic and biological environments.

Previous studies have extensively studied the influences of monovalent and divalent salts as well as natural organic matters (NOM) on the aggregation kinetics, fate, and transport of nanomaterials (52-55). Our work indicates that aerobic and anaerobic conditions also influence the aggregation behaviors of AgNPs, and our results suggest that AgNPs tend to aggregate slowly under anaerobic conditions and may appear as nanoparticles (instead of aggregates) for a long residence time. These findings are important for understanding the aggregation behaviors of AgNPs in the typical solution chemistries of aquatic environments. Moreover, anaerobic environments not only are common in natural environments (e.g., deep soils and underground water) but also are important in biological systems such as the human GI tract. Therefore, this study may lay out the ground work for understanding the potential fate and transformation of AgNPs in biological fluids or with biological interfaces. Meanwhile, it is also imperative to conduct a systematic fundamental study of aggregation behavior in biosystems and to gain insights about potential implications for human health.

3. Cellular and subcellular impairment by exposure to NPs

Imaging and quantifying interfacial interactions between NPs and biological surfaces is critical to gain information that will benefit both applications of nanotechnology and understanding of its potential environmental impact. In this regard, we also extend our research into the biological interactions with metal oxides NPs and the following two sections briefly introduce our preliminary results on cellular and genetic level impacts from NP exposure.

3.1. Surface disruption of *E. coli* cells after exposure to hematite NPs

As we previously reported, NP exposure led to surface disruption on the human intestinal cell line (Caco-2) (56). The results in Figure 9 demonstrated how individual hematite NPs interacted with live *E. coli* cells through AFM imaging. The AFM images provided a striking visualization of the adsorption of hematite NPs onto *E. coli* cells and the subsequent disruption in their extracellular appendages (flagella). The surface potential of *E. coli* cells dropped significantly from approximately -100 mV to -600 mV, with the adsorption of hematite NPs (results are not shown here). These findings will lead to a more thorough knowledge of nano-bio interfacial interaction mechanisms and allow us to establish criteria for designing environmentally benign semiconductor nanomaterials.

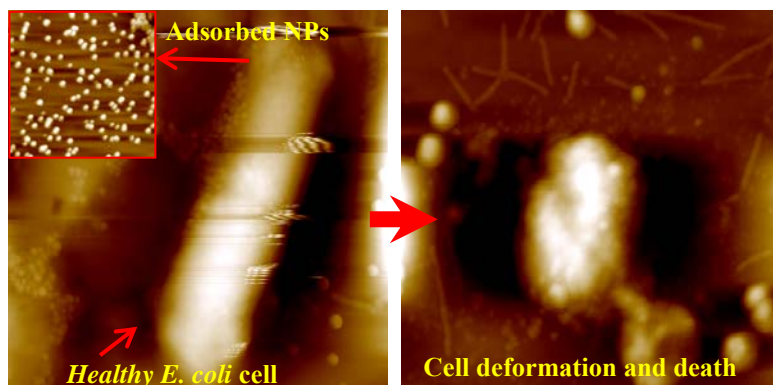


Figure 9 Exposure impacts of hematite NPs on *E. coli* cells.

3.2. Subcellular impairment at the genetic level

At subcellular level, our recent publication indicated that after the exposure, ultras-small NPs (e.g., QDs) have opportunities to permeate into *E. coli* cells (57), probably through diffusion across cell membranes (58), endocytosis (59), and/or non-phagocytic mechanisms (60). This study examined the binding of QDs with *E. coli* DNA *in vitro* and *in vivo*. With the unique function, KFM demonstrated its ability to determine the morphological and electrical changes in DNA after exposure to QDs as well as to distinguish individual QDs from DNA matrices. The results in Figure 10 indicate that nonspecific binding with QDs led to transformation of linear DNA into pearl-like spheres. *In vivo* experiments showed that QDs could permeate into *E. coli* cells and bind to genomic DNA. To the best of our knowledge, this is the first successful demonstration of the use of KFM to detect single QD-DNA binding. KFM potentially can be used in characterization of nanomaterials and their interfacial interactions with biomolecular matrices.

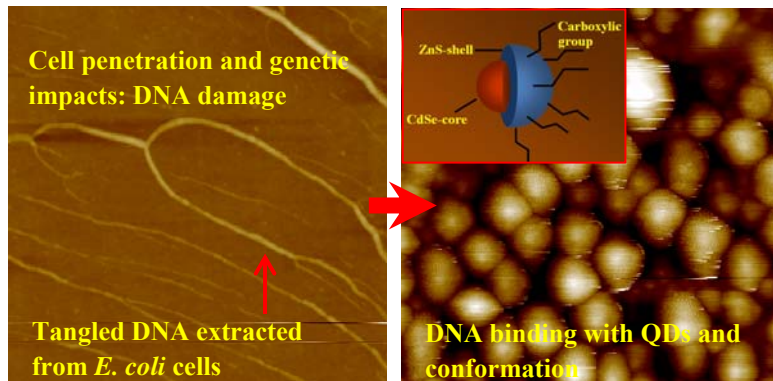


Figure 10 DNA binding with QDs and the shift in their conformation from linear to spherical.

Reference:

- (1) Hasselov, M.; Readman, J. W.; Ranville, J. F.; Tiede, K. Nanoparticle analysis and characterization methodologies in environmental risk assessment of engineered nanoparticles. *Ecotoxicology* **2008**, *17* (5), 344-61.
- (2) Darlington, T. K.; Neigh, A. M.; Spencer, M. T.; Nguyen, O. T.; Oldenburg, S. J. Nanoparticle characteristics affecting environmental fate and transport through soil. *Environ Toxicol Chem* **2009**, *28* (6), 1191-1199.
- (3) Klaine, S. J.; Alvarez, P. J. J.; Batley, G. E.; Fernandes, T. F.; Handy, R. D.; Lyon, D. Y.; Mahendra, S.; McLaughlin, M. J.; Lead, J. R. Nanomaterials in the environment: behavior, fate, bioavailability, and effects. *Environ. Toxicol. Chem.* **2008**, *27* (9), 1825-1851
- (4) Zhang, Y.; Chen, Y. S.; Westerhoff, P.; Crittenden, J. Impact of natural organic matter and divalent cations on the stability of aqueous nanoparticles. *Water Res.* **2009**, *43* (17), 4249-4257.
- (5) Nurmi, J. T.; Tratnyek, P. G.; Sarathy, V.; Baer, D. R.; Amonette, J. E.; Pecher, K.; Wang, C.; Linehan, J. C.; Matson, D. W.; Penn, R. L.; Driessen, M. D. Characterization and properties of metallic iron nanoparticles: spectroscopy, electrochemistry, and kinetics. *Environ. Sci. Technol.* **2005**, *39* (5), 1221-1230.
- (6) Murdock, R. C.; Braydich-Stolle, L.; Schrand, A. M.; Schlager, J. J.; Hussain, S. M. Characterization of nanomaterial dispersion in solution prior to in vitro exposure using dynamic light scattering technique. *Toxicol. Sci.* **2008**, *101* (2), 239-253.
- (7) Marambio-Jones, C.; Hoek, E. M. V. A review of the antibacterial effects of silver nanomaterials and potential implications for human health and the environment. *J. Nanopart. Res.* **2010**, *12* (5), 1531-1551.
- (8) Pal, S.; Tak, Y. K.; Song, J. M. Does the antibacterial activity of silver nanoparticles depend on the shape of the nanoparticle? A study of the gram-negative bacterium *Escherichia coli*. *Appl. Environ. Microbiol.* **2007**, *73* (6), 1712-1720.
- (9) Panyala, N. R.; Pena-Mendez, E. M.; Havel, J. Silver or silver nanoparticles: a hazardous threat to the environment and human health? *J. Appl. Biomed.* **2008**, *6* (3), 117-129.
- (10) Zhang, Y.; Chen, Y.; Westerhoff, P.; Hristovski, K.; Crittenden, J. C. Stability of commercial metal oxide nanoparticles in water. *Water Res.* **2008**, *42* (8-9), 2204-2212.
- (11) Benn, T. M.; Westerhoff, P. Nanoparticle silver released into water from commercially available sock fabrics. *Environ. Sci. Technol.* **2008**, *42* (11), 4133-4139.
- (12) Chen, C. Y.; Chiang, C. L. Preparation of cotton fibers with antibacterial silver nanoparticles. *Mater. Lett.* **2008**, *62* (21-22), 3607-3609.
- (13) Choi, O.; Yu, C.-P.; Esteban Fernández, G.; Hu, Z. Interactions of nanosilver with *Escherichia coli* cells in planktonic and biofilm cultures. *Water Research* **2010**, *In Press, Corrected Proof*.
- (14) Morones, J. R.; Elechiguerra, J. L.; Camacho, A.; Holt, K.; Kouri, J. B.; Ramirez, J. T.; Yacaman, M. J. The bactericidal effect of silver nanoparticles. *Nanotechnology* **2005**, *16* (10), 2346-2353.
- (15) Navarro, E.; Piccapietra, F.; Wagner, B.; Marconi, F.; Kaegi, R.; Odzak, N.; Sigg, L.; Behra, R. Toxicity of Silver Nanoparticles to *Chlamydomonas reinhardtii*. *Environ. Sci. Tech.* **2008**, *42* (23), 8959-8964.
- (16) Asharani, P. V.; Wu, Y. L.; Gong, Z. Y.; Valiyaveetil, S. Toxicity of silver nanoparticles in zebrafish models. *Nanotechnology* **2008**, *19* (25), 8.
- (17) Arora, S.; Jain, J.; Rajwade, J. M.; Paknikar, K. M. Interactions of silver nanoparticles with primary mouse fibroblasts and liver cells. *Toxicol. Appl. Pharmacol.* **2009**, *236* (3), 310-318.
- (18) Ahamed, M.; Siddiqui, M. A.; Akhtar, M. J.; Ahmad, I.; Pant, A. B.; Alhadlaq, H. A. Genotoxic potential of copper oxide nanoparticles in human lung epithelial cells. *Biochem. Biophys. Res. Commun.* **2010**, *396* (2), 578-583.
- (19) AshaRani, P. V.; Mun, G. L. K.; Hande, M. P.; Valiyaveetil, S. Cytotoxicity and Genotoxicity of Silver Nanoparticles in Human Cells. *ACS Nano* **2009**, *3* (2), 279-290.
- (20) Wise, S. S.; Mason, M. D.; Holmes, A. H.; Savery, L. C.; Li, C. T.; Goodale, B. C.; Shaffiey, F.; Wise, J. P.; Craig, G.; Walter, R. B.; Payne, R.; Kerr, I. A. R.; Spaulding, M.; Wise, J. P. Cytotoxicity and genotoxicity of silver nanoparticles in human and marine cell lines. *Environ. Mol. Mutag.* **2007**, *48* (7), 606-606.
- (21) Ji, Z.; Jin, X.; George, S.; Xia, T.; Meng, H.; Wang, X.; Suarez, E.; Zhang, H.; Hoek, E. M. V.; Godwin, H.; Nel, A. E.; Zink, J. I. Dispersion and Stability Optimization of TiO₂ Nanoparticles in Cell Culture Media. *Environ. Sci. Technol.* **2010**, *44* (19), 7309-7314.

- (22) Keller, A. A.; Wang, H.; Zhou, D.; Lenihan, H. S.; Cherr, G.; Cardinale, B. J.; Miller, R.; Ji, Z. Stability and Aggregation of Metal Oxide Nanoparticles in Natural Aqueous Matrices. *Environmental Science & Technology* **2010**, *44* (6), 1962-1967.
- (23) Hoek, E. M. V.; Bhattacharjee, S.; Elimelech, M. Effect of Membrane Surface Roughness on Colloid membrane DLVO Interactions. *langmuir* **2003**, *19* (11), 4836-4847.
- (24) Richard Bowen, W.; Doneva, T. A. Atomic force microscopy studies of nanofiltration membranes: surface morphology, pore size distribution and adhesion. *Desalination* **2000**, *129* (2), 163-172.
- (25) Elimelech, M.; O'Melia, C. R. Kinetics of deposition of colloidal particles in porous media. *Environ. Sci. Tech.* **2002**, *24* (10), 1528-1536.
- (26) Elimelech, M.; Xiaohua, Z.; Childress, A. E.; Seungkwan, H. Role of membrane surface morphology in colloidal fouling of cellulose acetate and composite aromatic polyamide reverse osmosis membranes. *J. Membr. Sci.* **1997**, *127* (1), 101-109.
- (27) Hirose, M.; Ito, H.; Kamiyama, Y. Effect of skin layer surface structures on the flux behaviour of RO membranes. *J. Membr. Sci.* **1996**, *121* (2), 209-215.
- (28) Bhattacharjee, S.; Kim, A. S.; Elimelech, M. Concentration Polarization of Interacting Solute Particles in Cross-Flow Membrane Filtration. *J. Colloid Interface Sci.* **1999**, *212* (1), 81-99.
- (29) Hirose, M.; Ito, H.; Kamiyama, Y. Effect of skin layer surface structures on the flux behaviour of RO membranes. *Journal of Membrane Science* **1996**, *121* (2), 209-215.
- (30) Sun, N.; Walz, J. Y. A model for calculating electrostatic interactions between colloidal particles of arbitrary surface topology. *Journal of Colloid and Interface Science* **2001**, *234* (1), 90-105.
- (31) Hermansson, M. The DLVO theory in microbial adhesion. *Colloids Surf., B* **1999**, *14* (1-4), 105-119.
- (32) Bacchin, P.; Aimar, P.; Sanchez, V. Influence of surface interaction on transfer during colloid ultrafiltration. *J. Membr. Sci.* **1996**, *115* (1), 49-63.
- (33) Pujar, N. S.; Zydney, A. L. Electrostatic effects on protein partitioning in size-exclusion chromatography and membrane ultrafiltration. *J. Chromatogr. A* **1998**, *796* (2), 229-238.
- (34) Behrens, S. H.; Christl, D. I.; Emmerzael, R.; Schurtenberger, P.; Borkovec, M. Charging and Aggregation Properties of Carboxyl Latex Particles: Experiments versus DLVO Theory. *langmuir* **2000**, *16* (6), 2566-2575.
- (35) Chen, K. L.; Elimelech, M. Aggregation and deposition kinetics of fullerene (C-60) nanoparticles. *langmuir* **2006**, *22* (26), 10994-11001.
- (36) Ryan, J. N.; Elimelech, M. Colloid mobilization and transport in groundwater. *Colloids Surf., A* **1996**, *107*, 1-56.
- (37) Holthoff, H.; Borkovec, M.; Schurtenberger, P. Determination of light-scattering form factors of latex particle dimers with simultaneous static and dynamic light scattering in an aggregating suspension. *Phys. Rev. E: Stat. Phys., Plasmas, Fluids*, **1997**, *56* (6), 6945-6953.
- (38) Holthoff, H.; Schmitt, A.; FernandezBarbero, A.; Borkovec, M.; CabrerizoVilchez, M. A.; Schurtenberger, P.; HidalgoAlvarez, R. Measurement of absolute coagulation rate constants for colloidal particles: Comparison of single and multiparticle light scattering techniques. *J. Colloid Interface Sci.* **1997**, *192* (2), 463-470.
- (39) Yang, J.; Hand, D. W.; Hokanson, D. R.; Crittenden, J. C. Application of an isothermal, three-phase catalytic reactor model to predict unsteady-state fixed-bed performance. *Environ. Sci. Tech.* **2003**, *37* (2), 428-436.
- (40) Trinh, L. T. T.; Kjoniksen, A. L.; Zhu, K. Z.; Knudsen, K. D.; Volden, S.; Glomm, W. R.; Nystrom, B. Slow salt-induced aggregation of citrate-covered silver particles in aqueous solutions of cellulose derivatives. *Colloid and Polymer Science* **2009**, *287* (12), 1391-1404.
- (41) Throckback, I. N.; Johansson, M.; Rosenquist, M.; Pell, M.; Hansson, M.; Hallin, S. Silver (Ag⁺) reduces denitrification and induces enrichment of novel nirK genotypes in soil. *FEMS Microbiol. Lett.* **2007**, *270* (2), 189-194.
- (42) Chen, X.; Schluesener, H. J. Nanosilver: A nanoparticle in medical application. *Toxicol. Lett.* **2008**, *176* (1), 1-12.
- (43) Braydich-Stolle, L.; Hussain, S.; Schlager, J. J.; Hofmann, M. C. In vitro cytotoxicity of nanoparticles in mammalian germline stem cells. *Toxicol. Sci.* **2005**, *88* (2), 412-419.

- (44) Sung, J. H.; Ji, J. H.; Yoon, J. U.; Kim, D. S.; Song, M. Y.; Jeong, J.; Han, B. S.; Han, J. H.; Chung, Y. H.; Kim, J.; Kim, T. S.; Chang, H. K.; Lee, E. J.; Lee, J. H.; Yu, I. J. Lung function changes in Sprague-Dawley rats after prolonged inhalation exposure to silver nanoparticles. *Inhal. Toxicol.* **2008**, *20* (6), 567-574.
- (45) Liu, J. Y.; Hurt, R. H. Ion Release Kinetics and Particle Persistence in Aqueous Nano-Silver Colloids. *Environ. Sci. Tech.* **2010**, *44* (6), 2169-2175.
- (46) Jin, X.; Li, M.; Wang, J.; Marambio-Jones, C.; Peng, F.; Huang, X.; Damoiseaux, R.; Hoek, E. M. V. High-Throughput Screening of Silver Nanoparticle Stability and Bacterial Inactivation in Aquatic Media: Influence of Specific Ions. *Environ. Sci. Technol.* **2010**, *44* (19), 7321-7328.
- (47) Buettner, K. M.; Rinciog, C. I.; E.Mylon, S. Aggregation Kinetics of Cerium Oxide Nanoparticles in Monovalent and Divalent Electrolytes. *Colloids Surf., A* **2010**, *366* (1-3), 74-79.
- (48) Chen, K. L.; Mylon, S. E.; Elimelech, M. Aggregation kinetics of alginate-coated hematite nanoparticles in monovalent and divalent electrolytes. *Environ. Sci. Tech.* **2006**, *40* (5), 1516-1523.
- (49) Sharma, V. K. Aggregation and toxicity of titanium dioxide nanoparticles in aquatic environment-A Review. *Journal of Environmental Science and Health Part a-Toxic/Hazardous Substances & Environmental Engineering* **2009**, *44* (14), 1485-1495.
- (50) He, Y. T.; Wan, J. M.; Tokunaga, T. Kinetic stability of hematite nanoparticles: the effect of particle sizes. *J. Nanopart. Res.* **2008**, *10* (2), 321-332.
- (51) Kallay, N.; Zalac, S. Stability of nanodispersions: a model for kinetics of aggregation of nanoparticles. *J. Colloid Interface Sci.* **2002**, *253* (1), 70-76.
- (52) Van Hoecke, K.; Quik, J. T. K.; Mankiewicz-Boczek, J.; De Schampelaere, K. A. C.; Elsaesser, A.; Van der Meeren, P.; Barnes, C.; McKerr, G.; Howard, C. V.; Van De Meent, D.; Ryzdzynski, K.; Dawson, K. A.; Salvati, A.; Lesniak, A.; Lynch, I.; Silversmit, G.; De Samber, B.; Vincze, L.; Janssen, C. R. Fate and Effects of CeO₂ Nanoparticles in Aquatic Ecotoxicity Tests. *Environ. Sci. Tech.* **2009**, *43* (12), 4537-4546.
- (53) Saleh, N. B.; Pfefferle, L. D.; Elimelech, M. Influence of Biomacromolecules and Humic Acid on the Aggregation Kinetics of Single-Walled Carbon Nanotubes. *Environ. Sci. Tech.* **2010**, *44* (7), 2412-2418.
- (54) Li, Z. Q.; Greden, K.; Alvarez, P. J. J.; Gregory, K. B.; Lowry, G. V. Adsorbed Polymer and NOM Limits Adhesion and Toxicity of Nano Scale Zerovalent Iron to *E. coli*. *Environ. Sci. Tech.* **2010**, *44* (9), 3462-3467.
- (55) Petosa, A. R.; Jaisi, D. P.; Quevedo, I. R.; Elimelech, M.; Tufenkji, N. Aggregation and Deposition of Engineered Nanomaterials in Aquatic Environments: Role of Physicochemical Interactions. *Environ. Sci. Technol.* **2010**, *44* (17), 6532-6549.
- (56) Zhang, W.; Kalive, M.; Capco, D. G.; Chen, Y. Adsorption of hematite nanoparticles onto Caco-2 cells and the cellular impairments: effect of particle size *Nanotechnology* **2010**, *21* (35), 355103.
- (57) Zhang, W.; Yao, Y.; Chen, Y. Imaging and Quantifying the Morphology and Nanoelectrical Properties of Quantum Dot Nanoparticles Interacting with DNA. *J. Phys. Chem. C* **2010**, DOI:10.1021/jp107676h.
- (58) Lin, S. J.; Keskar, G.; Wu, Y. N.; Wang, X.; Mount, A. S.; Klaine, S. J.; Moore, J. M.; Rao, A. M.; Ke, P. C. Detection of phospholipid-carbon nanotube translocation using fluorescence energy transfer. *Appl. Phys. Lett.* **2006**, *89* (14), 143118-143121.
- (59) Lee, J. K. Toxicity and tissue distribution of magnetic nanoparticles in mice. *Toxicol. Sci.* **2006**, *90* (1), 267-267.
- (60) Geiser, M.; Rothen-Rutishauser, B.; Kapp, N.; Schurch, S.; Kreyling, W.; Schulz, H.; Semmler, M.; Hof, V. I.; Heyder, J.; Gehr, P. Ultrafine particles cross cellular membranes by nonphagocytic mechanisms in lungs and in cultured cells. *Environ. Health Perspect.* **2005**, *113* (11), 1555-1560.

PART II. Benchmark data describing relationship between physicochemical properties and bilayer assay

Summary/Abstract:

Quantitative structure-activity relationships (QSARs) relate the physicochemical characteristics of NPs to their biological toxicity and have the potential to predict the toxic effects and bioaccumulation of existing and future engineered NPs used in semiconductor industries. NP toxicity and bioaccumulation are typically measured by a series of in-vitro cell culture protocols and by animal exposure tests. Investigating the relationships between the toxicity and bioaccumulation of NPs and their physicochemical properties (composition, size, geometry, charge, and molecular structure) is a significant step toward understanding and predicting potential risks of nanomaterials. Although the QSAR model has been used successfully for decades in classifying hazardous chemicals and for environmental risk assessment, their use in predicting toxicity and bioaccumulation of NPs is relatively new due to the lack of physicochemical data required to create a useful model.

Considering the wide range of nanoparticles' properties and diversity of animal and in-vitro models, it is challenging to map the detailed physicochemical properties of nanoparticles to the empirical bioaccumulation and toxicology studies. For organic contaminants, global descriptors such as the partitioning between the organic solvent phases (typically n-octanol) and water (K_{OW}) has traditionally been used as an empirical approach to evaluate the bioavailability (and from this infer toxicology) of organic pollutants and is used extensively in current EPA models.

In our work, we aim to develop analogous global descriptor methods for predicting bioaccumulation and toxicity of nanoparticles that account for the collective influence of nanoparticle properties, in a similar way as K_{OW} depends upon multiple parameters of organic pollutants (molecular weight, conformation, hydration states, ionic charge, etc). In this talk we quantify nanoparticle's lipid-water distribution coefficients and disruption of bilayers and use them as a global descriptor that captures the critical interactions between nanoparticles and biological interfaces which may be used to predict their bioaccumulation and toxicity potential.

To develop a robust QSAR model capable of predicting the toxicity of semiconductor nanomaterials, this report summarizes recent experimental results focusing on developing global descriptor for nanoparticles bioaccumulation and toxicity using lipid bilayer based assays. The bilayer assay measures the distribution of nanoparticles between water and a bilayer surface in the goal of developing a **predictive** empirical method for predicting NP bioaccumulation in organisms.

Technical Results and Data:

The partitioning of organic pollutants between octanol and water (K_{ow}) traditionally has been used as an empirical approach to evaluate the fate and bioaccumulation potential of organic pollutants (5, 6) and is used extensively in current EPA ecotoxicity models such as EPI Suite, ECOSAR, and AQUATOX. Characterization of ENMs often involves numerous physical and chemical measurements of size distribution, shape, aqueous zeta potential, surface functionality, surface area, etc. However, it is challenging to transition from these precise measurements to models suitable to assess the fate and bioavailability of ENMs in the environment, especially in complex matrices. Global descriptor methods such as partitioning have begun to be employed for ENMs. K_{ow} recently was determined for carbon nanotubes (7), C_{60} (8), and dendrimers (9). These measurements provide valuable insights into the relevancy of K_{ow} to the fate, transport, and bioaccumulation potential of ENMs. However, we and others (9, 10) have observed that ENMs in octanol-water systems can accumulate at interfaces and form emulsions that complicate the design, quantification, and interpretation of K_{ow} experiments and thus their use in predictive models. There is an opportunity to

develop quantitative approaches for predicting bioaccumulation of ENMs that account for the collective influence of ENM properties in a manner similar to the way in which K_{ow} or lipid-water partitioning depends upon single or multiple parameters of organic pollutants such as molar volume, aqueous solubility, and acidity constants (11-13).

Synthetic lipid bilayers, which mimic natural biological membranes, have been used increasingly as replacements for octanol in partitioning studies. The lipid bilayer-water distribution coefficient (K_{lipw}) has been shown to be a more appropriate descriptor than K_{ow} for the biological membrane uptake of some classes of hydrophobic (11,14, 15) and ionizable organic pollutants (16) as well as surfactants (17). The thermodynamics of fish lipid-water and simulated biological membrane-water partitioning is different from octanol-water partitioning. The disparity is thought to originate from the highly organized structure of biological membranes as opposed to bulk solvent octanol (15, 18). We hypothesize that the ionizable surfaces of some ENMs may be analogous to ionizable organic pollutants, and as such K_{lipw} may be more valuable than K_{ow} in prediction of bioaccumulation. Lipid bilayers' mass is nearly all at the interface and can be quantified, eliminating the difficulty encountered in the octanol-water partitioning of surface-active compounds and potentially some types of ENMs that may also partition to interfaces. The most widely used technique to determine lipid bilayer-water distribution coefficients is the equilibrium dialysis method in which water and a liposome suspension (i.e., lipid bilayer vesicles) are separated by a dialysis membrane that allows the diffusion of chemicals but not the liposomes (14, 16, 17, 19-22). However, using dialysis membranes to separate the water and liposomes may hinder ENM diffusion and promote mass losses considering that unilamellar liposomes generally have sizes <100 nm, close to those of ENMs.

In this work, we examine the lipid bilayer-water distribution behaviors of ENMs using solid-supported lipid membranes (SSLMs) (23, 24) with the goal of developing a quantitative method for assessing the interaction at this critical nano-biological interface (25). We use commercial lipid bilayers noncovalently coated on silica spheres, which offer the advantage that the relatively dense SSLMs can be separated easily from free ENMs by gravitational settling. SSLMs have been used in partitioning studies of pharmaceutical compounds (24) and organic acids (19), and the results are consistent with those obtained by the equilibrium dialysis method. We selected nC₆₀ and polyhydroxylated C₆₀ (i.e., fullerol) for lipid bilayer-water distribution tests because nC₆₀ and fullerol are the focus of recent ecotoxicology, fate, and transport studies (1), and fullerol-like C₆₀ derivatives are potential transformation products of nC₆₀ in the aquatic environments (26-28). Cerium oxide nanoparticles are used because they are a representative of the particles used in chemical mechanical polishing and selected for the round robin within the ERC. We show that the particles exhibit pseudo-equilibrium distributions between water and lipid bilayers after equilibration and can be fit using conventional nonlinear Langmuir or Freundlich isotherm models. The accumulation of cerium and fullerene nanoparticles in the lipid bilayers increases as pH decreases, consistent with the increased zeta potential magnitude (i.e., less negative) of nanoparticles and lipid bilayers. Finally, the results from the SSLM and ENM interaction studies are compared with recent bioaccumulation and toxicity studies using aquatic organisms.

Interaction Kinetics

The interaction kinetics studies of particles with SSLM are shown in Figure 2. nC₆₀ (6.5 mg/L) reached pseudo-equilibrium after mixing with SSLM (0.46 mM lipid) for 9 h at pH = 7.4, losing 25% of its mass to SSLMs (Figure 2a, solid symbols). We found that the kinetics is pH dependent. At pH = 5, the nC₆₀ (6.5 mg/L) reached pseudo-equilibrium in 30 h, losing 75% of its initial concentration. Some of the initial loss was due to nC₆₀ sorption to walls of the vials. For example, nC₆₀ in control samples (Figure 2a, open symbols) without SSLM present decreased by 25 and 35% of its initial concentrations at pH = 7.4 and 5,

respectively, due to loss to vial walls. We analyzed the nC_{60} concentration after shaking control vials, thus ruling out the loss as being due to sedimentation. The as-prepared nC_{60} size remained constant after 20 h of mixing with electrolytes at both pH values (data not shown), but the zeta potential changed from -54 mV to -31 mV and from -40 mV to -14 mV for pH values of 7.4 and 5, respectively. The reduction in zeta potential may be attributed to the presence of counter ions in the electrolyte (i.e., H^+ , Na^+ and K^+), that screen the surface charge. The greater decrease in the electrostatic repulsion between lipid bilayers and nC_{60} at pH = 5, based on the zeta potential change, may explain the faster interaction rate.

Cerium reaching equilibrium in less than five hours losing roughly 20% of its mass to the bilayers. The control samples were stable suggesting that no mass is lost to the vial walls. The size of the cerium remained constant over the experiment duration at roughly 90 nm.

The accumulation of fullerol in SSLMs reached pseudo-equilibrium more rapidly, in 2 h, showing negligible, 22, and 27% loss of initial concentrations at pH = 7.4, 5, and 3, respectively. Additional kinetic data varying initial fullerol concentrations from 26 to 86 mg/L at pH = 3 or 5 also show pseudo-equilibrium in 2 h (Figure S3). The fullerol concentrations in the control samples were stable, indicating no loss to the vial walls. The zeta potential of fullerol stayed relatively constant, slightly decreasing from -46 to -58 mV at pH = 5 and from -59 to -65 mV at pH = 7 during the period of equilibration, and its size was fairly constant at 150 nm.

Distribution Isotherms

The equilibrium distribution of nC_{60} , fullerol, and cerium oxide between SSLM and the aqueous phase in the pH range of 3 to 8.6 is presented in Figure 3; $C_{w, eq}$ spans nearly two orders of magnitude. nC_{60} accumulated in SSLMs to a greater degree at pH = 5 than 7.4. Fullerol also exhibits pH-dependent distribution behaviors with accumulation in SSLM increasing with decreasing pH. The nonlinearity between $C_{w, eq}$ and $C_{lip, eq}$ at higher concentrations may be attributed to the accumulation of nanoparticles on the SSLM surface and modification of the lipid surface charge characteristics leading to repulsion of like-charged nanoparticles. We estimate that nanoparticles cover $\leq 10\%$ of the SSLM total surface area at the highest nanoparticle dose used, assuming monolayer coverages. The cerium partitions onto the bilayer three times greater than fullerols at the same pH.

We use Langmuir and Freundlich isotherm models to fit the data because of the nonlinearity in distribution isotherms. Langmuir isotherms, such as those shown in Figure 4, display marginally better fits as measured using r-squared values. The Freundlich model fits are presented in Figure S4, and the fitting parameters of both models are summarized in Table 1. Although we tend to use the two isotherm models as empirical fitting tools for the data presented here, there are some interesting trends in the fitted parameters. The Freundlich adsorption capacity parameter (K_F) increases with decreasing pH and is consistent with the observed accumulation trends for nC_{60} and fullerol. The fullerol Freundlich adsorption intensity parameter (n), an indication of propensity to sorb additional adsorbates, decreases with increasing pH, indicating that it is more difficult for SSLM to accumulate additional fullerol at higher pH (34). Fullerol's Langmuir maximum accumulation capacity ($K_{lip, max}$) increases with decreasing pH in accord with the observed accumulation trend.

Environmental Implications

Bioconcentration factor (BCF), defined as chemical concentration measured in biota divided by chemical concentration measured in water, traditionally has been used to assess the bioaccumulation potential of chemicals (34). Tervonen et al. (35) recently reported the bioconcentration factors of nC_{60} measured using *Daphnia magna* as a test organism. They reported log BCFs of 3.3 to 3.8 (L/kg) at pH = 7,

which compares reasonably to our $\log K_{lipw} \approx 3.00$ (by the Langmuir model) and 3.14 to 3.30 (L/kg) (by the Freundlich model) for nC₆₀ at pH = 7.4 under similar exposure concentrations of 0.5 to 2 mg/L. In our previous work, we quantified the interactions of nC₆₀ and fullerol with heterotrophic bacteria wastewater biomass. We showed that nC₆₀ was removed by biosorption to the biomass to a greater extent than fullerol, which is qualitatively consistent with the current observations for SSLMs (36). Toxicity studies on human cell lines, bacteria, and fish indicate that nC₆₀ was more toxic than fullerol (37-39), consistent with the strong nC₆₀ interactions with lipid membranes observed in this work. No bioaccumulation studies have been conducted with cerium, so no comparison was made for that work.

This work presents the first quantitative study of the distribution of fullerene nanoparticles between lipid bilayers, which mimic natural biological membranes, and water. This is a potential first step toward the prediction of the bioaccumulation potential of ENMs. The findings from this work indicate that the lipid bilayer-water distribution of nC₆₀ and fullerol is a pseudo-equilibrium process that exhibits pH dependency in K_{lipw} . This observation is analogous to partitioning of ionizable organic pollutants. Our comparisons with organism bioaccumulation studies suggest that lipid bilayer-water distribution is a promising method for predicting the bioaccumulation potential of ENMs. Studies of ENMs with different core compositions, surface coatings, sizes, and shapes are needed and more quantitative research in determining BCFs using aquatic organisms in field studies or in simulated environments is critical to further validate the lipid bilayer-water distribution technique in the prediction of ENM bioaccumulation.

Supplementary Information:

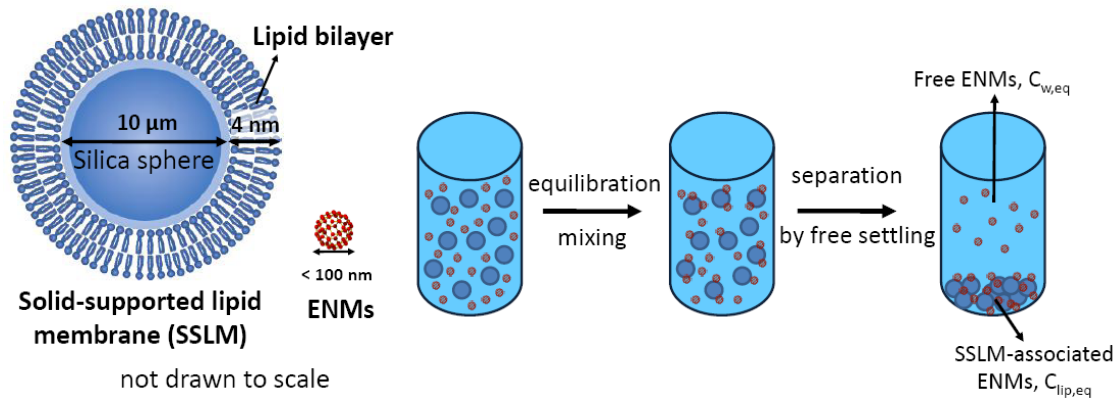


Figure 1. We are quantifying adsorption of ENM to lipid bilayers supported on 10 micron silica spheres. These commercially available solid-supported lipid membranes (SSLM) greatly improve the speed and accuracy of measurements and enable the quantification of lipid surface area. Varied concentrations of SSLM and ENMs are placed in glass vials and mixed on a rotary mixer in an end-over-end action. At equilibrium, vials will be sit quiescently, allowing the SSLM beads to settle to the bottom and the supernatants containing free ENMs will be drawn for analysis of concentrations.

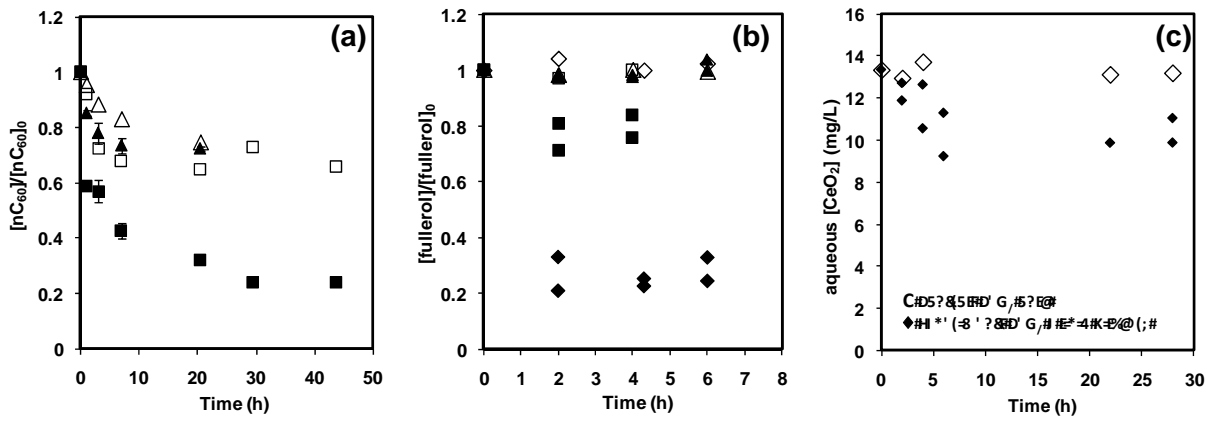


Figure 2. Interaction kinetics of nC_{60} (a), fullerol (b), and cerium oxide (c) with solid-supported lipid bilayer membranes (SSLMs), indicating the loss of NP in samples containing SSLM with $[\text{lipid}] = 0.47 \text{ mM}$ at $\text{pH} = 7.4$ (\blacktriangle), 5 (\blacksquare) or 3 (\blacklozenge) and in samples without SSLM at $\text{pH} = 7.4$ (\triangle), 5 (\square), or 3 (\lozenge). The initial nC_{60} concentration was 6.5 mg/L at $\text{pH} = 7.4$ and 5. The initial fullerol concentrations were 8.0, 11.0, and 11.0 mg/L at $\text{pH} = 7.4$, 5, and 3, respectively.

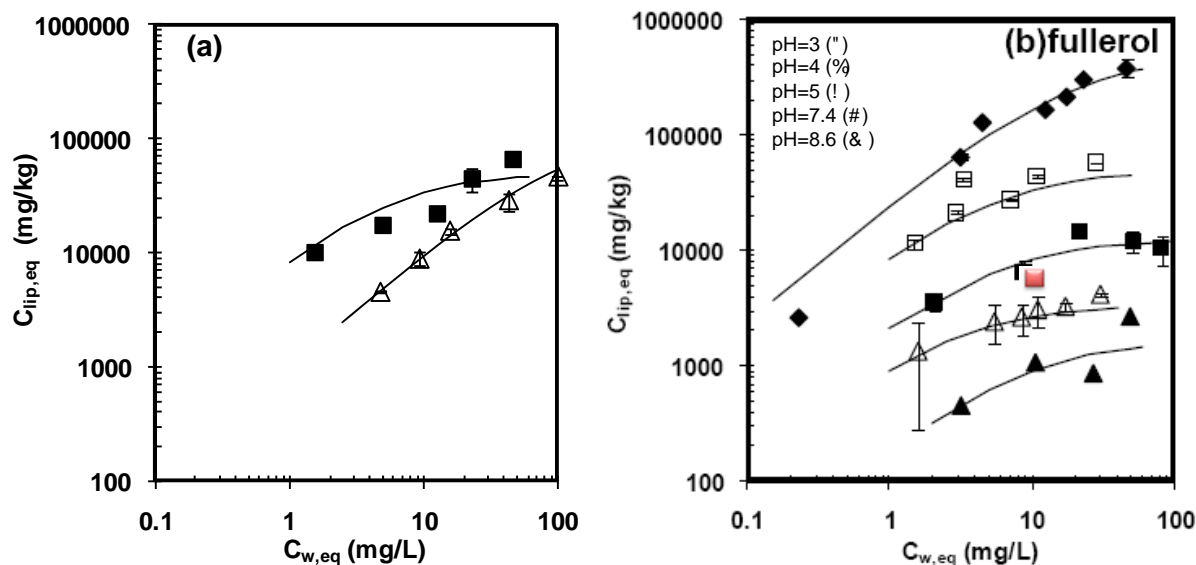


Figure 3. Distribution of nC_{60} (a) and fullerol and cerium oxide (b) between water and solid-supported lipid bilayers, indicating the isotherms at pH = 3 (\blacklozenge), 4 (\square), 5 (\blacksquare), 7.4 (\triangle), and 8.6 (\blacktriangle). The red square shows the cerium oxide NP. Lines represent the fit of Langmuir isotherms to the experimental data. Error bars indicate one standard deviation. Standard deviations of some data points are smaller than the symbols. The standard deviations for experimental data at pH = 8.6 were not plotted, as the values become negative, which is not valid in logarithmic plots, but the standard deviations are in the range of 600-1700.

References:

1. Klaine, S.J.; Alvarez, P. J. J.; Batley, G. E.; Fernandes, T. F.; Handy, R. D.; Lyon, D. Y.; Mahendra, S.; McLaughlin, M. J.; Lead, J. R. Nanomaterials in the environment: behavior, fate, bioavailability, and effects. *Environ. Toxicol. Chem.* **2008**, *27*, 1825-1851.
2. An inventory of nanotechnology-based consumer products currently on the market of the Project of Emerging Nanotechnology. Available at <http://www.nanotechproject.org/inventories/consumer/>. Accessed in November 2010.
3. Maynard, A. D.; Aitken, R. J.; Butz, T.; Colvin, V.; Donaldson, K.; Oberdorster, G.; Philbert, M. A.; Ryan, J.; Seaton, A.; Stone, V.; Tinkle, S.S.; Tran, L.; Walker, N. J.; Warheit, D. B. Safe handling of nanotechnology. *Nature* **2006**, *444*, 267-269.
4. Alvarez, P. J. J.; Colvin, V.; Lead, J.; Stone, V. Research priorities to advance eco-responsible nanotechnology. *ACS Nano* **2009**, *3*, 1616-1619.
5. Neely, W. B.; Branson, D. R.; Blau, G. E.; Partition coefficient to measure bioconcentration potential of organic chemicals in fish. *Environ. Sci. Technol.* **1974**, *8*, 1113-1115.
6. Chiou, C. T.; Freed, V. H.; Schmedding, D. W.; Kohnert, R. L. Partition coefficient and bioaccumulation of selected organic chemicals. *Environ. Sci. Technol.* **1977**, *11*, 475-478.
7. Petersen, E. J.; Huang, Q.; Weber, W. J. Relevance of octanol-water distribution measurements to the potential ecological uptake of multi-walled carbon nanotubes. *Environ. Toxicol. Chem.* **2010**, *29*, 1106-1112.
8. Jafvert, C. T.; Kulkarni, P. P. Buckminsterfullerene's (C_{60}) octanol-water partition coefficient (K_{ow}) and aqueous solubility. *Environ. Sci. Technol.* **2008**, *42*, 5945-5950.

9. Giri, J.; Diallo, M. S.; Goddard III, W. A.; Dalleska, N. F.; Fang, X.; Tang, Y. Partitioning of Poly(amidoamine) dendrimers between n-octanol and water. *Environ. Sci. Technol.* **2009**, *43*, 5123-5129.
10. Binks, B. P.; Rodrigues, J. A.; Inversion of emulsions stabilized solely by ionizable nanoparticles. *Angew. Chem. Int. Ed.* **2005**, *44*, 441-444.
11. Dulfer, W. J.; Govers, H. A. J.; Membrane-water partitioning of polychlorinated biphenyls in small unilamellar vesicles of four saturated phosphatidylcholines. *Environ. Sci. Technol.* **1995**, *29*, 2548-2554.
12. Chiou, C. T.; Schmedding, D. W.; Manes, M. Partitioning of organic compounds in octanol-water systems. *Environ. Sci. Technol.* **1982**, *16*, 4-10.
13. Jafvert, C. T.; Westall, J. C.; Grieder, E.; Schwarzenbach, R. P. Distribution of hydrophobic ionogenic organic compounds between octanol and water: Organic acids. *Environ. Sci. Technol.* **1990**, *24*, 1795-1803.
14. Kwon, J. H.; Liljestrand, H. M.; Katz, L. E. Partitioning of moderately hydrophobic endocrine disruptors between water and synthetic membrane vesicles. *Environ. Toxicol. Chem.* **2006**, *25*, 1984-1992.
15. Opperhuizen, A.; Serne, P.; Van der Steen, J. M. D. Thermodynamics of fish/water and octan-1-ol/water partitioning of some chlorinated benzenes. *Environ. Sci. Technol.* **1988**, *22*, 286-292.
16. Escher, B. I.; Schwarzenbach, R. P. Partitioning of substituted phenols in liposome-water, biomembrane-water, and octanol-water systems. *Environ. Sci. Technol.* **1996**, *30*, 260-270.
17. Muller, M. T.; Zehnder, A. J.; Escher, B. I. Liposome-water and octanol-water partitioning of alcohol ethoxylates. *Environ. Toxicol. Chem.* **1999**, *18*, 2191-2198.
18. Kwon, J. H.; Liljestrand, H. M.; Katz, L. E. Partitioning thermodynamics of selected endocrine disruptors between water and synthetic membrane vesicles: Effects of membrane compositions. *Environ. Sci. Technol.* **2007**, *41*, 4011-4018.
19. Escher, B. I.; Schwarzenbach, R. P.; Westall, J. C. Evaluation of liposome-water partitioning of organic acids and bases. 2. Comparison of experimental determination methods. *Environ. Sci. Technol.* **2000**, *34*, 3962-3968.
20. Escher, B. I.; Schwarzenbach, R. P.; Westall, J. C. Evaluation of liposome-water partitioning of organic acids and bases. 1. Development of a sorption model. *Environ. Sci. Technol.* **2000**, *34*, 3954-3961.
21. Escher, B. I.; Berger, C.; Bramaz, N.; Kwon, J. H.; Richter, M.; Tsinman, O.; Avdeef, A. Membrane-water partitioning, membrane permeability, and baseline toxicity of the parasiticides ivermectin, albendazole, and morantel. *Environ. Toxicol. Chem.* **2008**, *27*, 909-918.
22. Yamamoto, H.; Liljestrand, H. M.; Partitioning of selected estrogenic compounds between synthetic membrane vesicles and water: Effects of lipid components. *Environ. Sci. Technol.* **2004**, *38*, 1139-1147.
23. Loidl-Stahlhofen, A.; Schmitt, J.; Noller, J.; Hartmann, T.; Brodowsky, H.; Schmitt, W.; Keldenich, J. Solid-supported biomolecules on modified silica surfaces-A Tool for fast physicochemical characterization and high-throughput screening. *Adv. Mater.* **2001**, *13*, 1829-1834.
24. Loidl-Stahlhofen, A.; Hartmann, T.; Schottner, M.; Rohring, C.; Brodowsky, H.; Schmitt, J.; Keldenich, J. Multilamellar liposomes and solid-supported lipid membranes (TRANSIL): screening of lipid-water partitioning toward a high-throughput scale. *Pharmaceut. Res.* **2001**, *18*, 1782-1788.
25. Nel, A. E.; Madler, L.; Velegol, D.; Xia, T.; Hoek, E. M. V.; Somasundaran, P.; Klaessig, F.; Castranova, V.; Thompson, M. Understanding biophysicochemical interactions at the nano-bio interface. *Nat. Mater.* **2009**, *8*, 543-557.
26. Hou, W.-C.; Jafvert, C. T. Photochemical transformation of aqueous C₆₀ clusters in sunlight. *Environ. Sci. Technol.* **2009**, *43*, 362-367.
27. Lee, J.; Cho, M.; Fortner, J. D.; Hughes, J. B.; Kim, J. Transformation of aggregated C₆₀ in the aqueous phase by UV irradiation. *Environ. Sci. Technol.* **2009**, *43*, 4878-4883.
28. Fortner, J. D.; Kim, D.; Boyd, A. M.; Falkner, J. C.; Moran, S.; Colvin, V. L.; Hughes, J. B.; Kim, J. Reaction of water-stable C₆₀ aggregates with ozone. *Environ. Sci. Technol.* **2007**, *41*, 7497-7502.

29. Hope, M. J.; Bally, M. B.; Webb, G.; Cullis, P. R. Production of large unilamellar vesicles by a rapid extrusion procedure. Characterization of size distribution, trapped volume and ability to maintain a membrane potential. *BBA-Biomembranes* **1985**, *812*, 55–65.
30. Petitou, M.; Tuy, F.; Rosenfeld, C. A simplified procedure for organic phosphorus determination from phospholipids. *Anal. Biochem.* **1978**, *91*, 350–353.
31. Hou, W.-C.; Jafvert, C. T. Photochemistry of aqueous C₆₀ clusters: Evidence of ¹O₂ formation and its role in mediating C₆₀ phototransformation. *Environ. Sci. Technol.* **2009**, *43*, 5257-5262.
32. Kucerka, N.; Kiselev, M. A.; Balgavy, P. Determination of bilayer thickness and lipid surface area in unilamellar dimyristoylphosphatidylcholine vesicles from small-angle neutron scattering curves: a comparison of evaluation methods. *Eur. Biophys. J.* **2003**, *33*, 328-334.
33. Zhou, Y.; Raphael, R. M. Solution pH alters mechanical and electrical properties of phosphatidylcholine membranes: relation between interfacial electrostatics, intramembrane potential, and bending elasticity. *Biophys. J.* **2007**, *92*, 2451–2462.
34. Schwarzenbach, R. P.; Gschwend, P. M.; Imboden, D. M. *Environmental Organic Chemistry*; John Wiley and Sons: New York, 2002.
35. Tervonen, K.; Waissi, G.; Petersen, E. J.; Akkanen, J.; Kukkonen, J. V. Analysis of fullerene-C₆₀ and kinetic measurements for its accumulation and depuration in *Daphnia magna*. *Environ. Toxicol. Chem.* **2010**, *29*, 1072-1078.
36. Kiser, M. A.; Ryu, H.; Jang, H.; Hristovski, K.; Westerhoff, P. Biosorption of nanoparticles to heterotrophic wastewater biomass. *Water Res.* **2010**, *44*, 4105-4114.
37. Sayes, C. M.; Fortner, J. D.; Guo, W.; Lyon, D.; Boyd, A. M.; Ausman, K. D.; Tao, Y. J.; Sitharaman B.; Wilson, L. J.; Hughes, J. B.; West, J. L.; Colvin, V. L. The differential cytotoxicity of water-soluble fullerenes. *Nano Lett.* **2004**, *4*, 1881-1887.
38. Zhu, X.; Zhu, L.; Duan, Z.; Chen, W.; Alvarez, P. J. J. Developmental toxicity in zebrafish (*Danio rerio*) embryos after exposure to manufactured nanomaterials: buckminsterfullerene aggregates (nC₆₀) and fullerol. *Environ. Toxicol. Chem.* **2007**, *26*, 976-979.
39. Usenko, C. Y.; Harper, S. L.; Tanguay, R. L. In vivo evaluation of carbon fullerene toxicity using embryonic zebrafish. *Carbon* **2007**, *45*, 1891-1898.
40. W-C. Hou, B.Y. Moghadam, P. Westerhoff, J.D. Posner. Distribution of Fullerene Nanomaterials between Water and Model Biological Membranes: Environmental Science and Technology, 2010, submitted.